Available online at www.sciencedirect.com
SCIENCE DIRECT®
Electrochimica Acta 50 (2005) 5200–5207
ELECTROCHIMICA Acta
www.elsevier.com/locate/electacta

Structural investigations of $LiFePO_4$ electrodes and in situ studies by Fe X-ray absorption spectroscopy

Aniruddha Deb [a,*], Uwe Bergmann [b], S.P. Cramer [c,d], Elton J. Cairns [a,e,1]

[a] *Environmental Energy Technologies Division, Lawrence Berkeley National Laboratory, Berkeley, CA 94720, USA*
[b] *Stanford Synchrotron Radiation Research Laboratory, Sand Hill Road, Menlo Park, CA 94025, USA*
[c] *Physical Bioscience Division, Lawrence Berkeley National Laboratory, Berkeley, CA 94720, USA*
[d] *Department of Applied Sciences, University of California, Davis, California, USA*
[e] *Department of Chemical Engineering, University of California, Berkeley, California, USA*

Received 30 November 2004; received in revised form 2 February 2005; accepted 2 February 2005
Available online 12 July 2005

Abstract

Fe K-edge X-ray absorption near edge spectroscopy (XANES) and extended X-ray absorption fine structure (EXAFS) have been performed on electrodes containing $LiFePO_4$ to determine the local atomic and electronic structure and their stability with electrochemical cycling. A versatile electrochemical in situ cell has been constructed for long-term soft and hard X-ray experiments for the structural investigation on battery electrodes during the lithium-insertion/extraction processes. The device is used here for an X-ray absorption spectroscopic study of lithium insertion/extraction in a $LiFePO_4$ electrode, where the electrode contained about 7.7 mg of $LiFePO_4$ on a 20 μm thick Al-foil. Fe K-edge X-ray absorption near edge spectroscopy (XANES) and extended X-ray absorption fine structure (EXAFS) have been performed on this electrode to determine the local atomic and electronic structure and their stability with electrochemical cycling. The initial state ($LiFePO_4$) showed iron to be in the Fe^{2+} state corresponding to the initial state (0.0 mAh) of the cell, whereas in the delithiated state ($FePO_4$) iron was found to be in the Fe^{3+} state corresponding to the final charged state (3 mAh). XANES region of the XAS spectra revealed a high spin configuration for the two states (Fe (II), d^6 and Fe (III), d^5). The results confirm that the olivine structure of the $LiFePO_4$ and $FePO_4$ is retained by the electrodes in agreement with the XRD observations reported previously. These results confirm that $LiFePO_4$ cathode material retains good structural short-range order leading to superior cycling capability.

Keywords: Fe K-edge; X-ray absorption near edge spectroscopy; Electrodes

1. Introduction

The emergence of portable telecommunications, computer equipment and, ultimately, electric and hybrid vehicles has created a growing demand for improvements in energy storage devices that are cost effective, operate for a longer time, and are smaller in size and weight [1]. Transition metal oxides have been investigated as active cathode materials because of their high potential versus Li/Li^+ and in many of the materials a large proportion of the lithium can be inserted/extracted reversibly.

Lithium insertion has been investigated in several Fe-containing compounds such as Li_3FeN_2 [2], $LiFe_5O_8$ [3], Fe_3O_4 [4], Fe_2O_3 [5] and $FePS_3$ [6]. These compounds rely on a Fe^{3+}/Fe^{2+} redox couple and hence have a low open-circuit voltage versus Li/Li^+. The substitution of oxygen by a polyanion MO_4^{3-} like sulfate or phosphate lowers the Fermi level of the Fe^{3+}/Fe^{2+} redox couple and thereby increases the cell potential [7–9]. This effect is more pronounced for compounds with fewer covalent Fe–O bonds, where M in MO_4^{3-} determines the strength of the Fe–O covalency via an inductive effect [10]. Since the demonstration of reversible

* Corresponding author. Fax: +1 510 486 7303.
E-mail address: adeb@lbl.gov (A. Deb).
[1] ISE member.

0013-4686/$ – see front matter © 2005 Elsevier Ltd. All rights reserved.
doi:10.1016/j.electacta.2005.02.086

electrochemical lithium insertion–extraction for $LiFePO_4$ in 1997 [11], lithium transition metal phosphates with an ordered olivine structure, $LiMPO_4$ (M = Co, Ni, Mn, Fe, Cu) have attracted much attention as promising new cathode materials for rechargeable lithium batteries [12–15]. One of the most promising candidates for rechargeable lithium cells is $LiFePO_4$, with a theoretical capacity of 170 mAh/g [11] and a voltage of >3.4 V versus Li/Li^+. $LiFePO_4$ is inexpensive, non-toxic, non-hygroscopic and environmentally friendly. It occurs in nature as the mineral triphylite, which has an orthorhombic unit cell (space group *Pmna*) [16] and often contains varying amounts of manganese as in $LiFe_xMn_{1-x}PO_4$. Both Li and M atoms are in octahedral sites with Li located in the 4a and M in the 4c positions. The oxygen atoms are nearly hexagonal closed-packed and the M atoms occupy zigzag chains of corner-shared octahedra running parallel to the *c*-axis in alternate *a*–*c* planes. These chains are bridged by corner- and edge-sharing PO_4^{3-} polyanions to form a host structure with strong three-dimensional bonding. The Li^+ ions in the 4a sites form continuous linear chains of edge-shared octahedra running parallel to the *c*-axis in the other *a*–*c* planes. The P_{tet}-O-Fe_{oct} linkage in the structure induces a superexchange interaction that tunes the Fe^{3+}/Fe^{2+} redox energy to useful levels (3.4 V) [11]. The stable nature of the olivine-type structure having a PO_4^{3-} polyanion with a strong P–O covalent bond provides not only excellent cycle-life but also a safe system. The fact that all oxygen atoms are not only bonded to Fe but also strongly bonded to phosphorous is advantageous for the safety of the battery since oxygen is less likely to be released at elevated temperature which makes oxygen ignition of the organic electrolyte an unlikely accident. Low utilization due to conductivity problems within the electrode and slow electron transfer kinetics at the iron phosphate retarded its application to start with. Special coatings, small grain size and substitution of part of the iron by other metals are concepts to ameliorate these unattractive properties. When the electrode is fully charged, the reactivity with regard to the combustion reaction with the organic electrolyte is low [15].

Synchrotron based X-ray absorption spectroscopy is a very useful tool to investigate the structural and electronic properties of electrode materials. X-ray absorption near edge spectroscopy (XANES) is an element-specific technique sensitive to the local atomic and electronic structure of the element of interest [17]. XANES and extended X-ray absorption fine-structure spectroscopic (EXAFS) studies have revealed details about the local coordination, site symmetry, oxidation state, and bond character in Mn oxides and Mn-containing molecular compounds [18–21]. In order to study the atomic and electronic structure of these materials and understand the changes occurring upon cycling, we performed in situ Fe XANES and EXAFS on this material. In the last few years the use of XAS in electrochemistry to study battery and fuel cell electrodes has gained momentum [22,23]. Recently XAS has been used to study catalyst on bifunctional oxygen diffusion electrodes containing $La_{1-x}Ca_xCoO_3$, which is used as a catalyst in these electrodes [24,25]. XAS studies on $Li_{1-x}Ni_{0.85}Co_{0.15}O_2$ and $Li_xNi_{0.8}Co_{0.2}O_2$ cathode materials were performed to elucidate the changes in the oxidation state, bond lengths and coordination numbers of these materials [26,27]. Though there have been many cell designs, which until now have been successfully tested for short-term experiments, very few studies exist wherein cells have been used for experiments which extend for several days or even a week. After overcoming many obstacles, a transmission in situ XAS study was performed on nickel oxide electrodes by McBreen et al. [28] to observe the change in structure during electrochemical oxidation. Due to the known limitations of in situ investigations e.g. difficult cycling set-up and complicated multi-element assembly of a working cell, these experiments are more complicated compared to ex situ measurements. A few workarounds have been developed by cycling and disassembling cells at appropriate electrochemical conditions, in this case a post mortem analysis is possible and the results may be substantially altered by examining states of the material which are not present under operating conditions. Upon charging and discharging a cell the lithium ions are extracted and inserted from the electrode material and this reaction is seriously limited by diffusion and may take hours to reach equilibrium. Since we are interested in studying the changes in the electrode material which may depend on the number of charge and discharge cycles, the experiments can last as long as several weeks or even months. Here we used an in situ cell that is reusable and utilizes kapton X-ray windows, is convenient to assemble in the glove box, and is portable. The effective design of the in situ cell allows us to cycle the cell for several weeks without any noticeable traces of corrosion of the lithium metal counter electrode. For a complete description and design of this novel electrochemical XAS cell the reader is referred to Deb at al. [29]. In contrast to the earlier work [29] where we have only considered the initial and the final states during charging, for our discussion here we have shown the results for the various states during the charging cycle, and have clearly shown how this promising material is changing during cycling. This has been done by studying the changes in the short-range order of the Fe–O and Fe–P distances at various stages of the charging cycle.

2. Experimental procedures

The $LiFePO_4$ powder used in this study was synthesized using the starting materials $Fe(NO_3)_3.9H_2O$ (iron nitrate, Aldrich), $Li(CH_3COO)_2.2H_2O$ (lithium acetate, Aldrich), H_3PO_4 (phosphoric acid, Sigma) and $HOCH_2COOH$ (glycolic acid, Aldrich). The metal compounds were first dissolved in phosphoric acid and deionized water. This solution was mixed until homogenous and was added to glycolic acid (1:2 metal:glycolic acid ratio). Ammonium

hydroxide was added to the solution to adjust the pH between 8.5 and 9.5. The solution was heated to 70–80 °C under N_2 until a gel was formed. This gel was then transferred to an alumina boat, heated slowly to 500 °C under flowing N_2, and then decomposed at that temperature for 10 h. The resultant powders were ground, dried, and then heated to 600 or 700 °C under a flow of N_2 gas, for 5–15 h. The reader is referred to Doeff et al. [30] for further details of the preparation of the electrodes containing $LiFePO_4$. The product was a single phase, as was verified by X-ray diffraction (XRD). The in situ cell was cycled galvanostatically using a Princeton Applied Research potentiostat/galvanostat (model Versa).

The X-ray absorption measurements, which included both XANES and EXAFS techniques, were performed on the bending magnet beam line DND-CAT of the Advanced Photon Source at Argonne National Laboratory, with 100 mA current at the top of the fill. A Si(1 1 1) double crystal monochromator was used for energy selection and the energy resolution of the monochromatic beam was determined to be about 1 eV as measured by the rocking curve width of the second crystal, while an active feedback loop maintained the peak reflectivity of the monochromator. The large harmonic content in the beam was rejected, by employing a platinum-coated mirror. All the measurements were recorded in the transmission mode using three ion chambers in series to measure the intensities of the incident beam I_0, the beam transmitted by the sample I_t and the beam subsequently transmitted by the reference foil I_{ref}. The intensities of the incident and the transmitted X-rays were monitored by nitrogen and helium filled ionization chambers. The monochromator was scanned in energy from 312 below to 1050 eV above the Fe K absorption edge (7112 eV). The Fe K-edge X-ray absorption spectra were measured in transmission mode at room temperature. Transmission ion chambers were used to measure the incident (I_0), transmitted (I_t), and reference (I_{ref}) signals. A 9 μm thick Fe foil was used as a reference, and both foil and I_{ref} detectors were positioned behind the sample along the direction [X-ray beam/I_0-detector/sample/I_{sample}-detector/Fe-foil/I_{ref}-detector]. Data were collected using a 0.1 eV step size through the edge region and a variable step size, giving $\Delta k_{max} = 0.05$ Å^{-1} for the EXAFS region. Reduction of the absorption data was performed using the EXAFSPAK analysis package available from SSRL. Transmission data from scans of each sample were averaged and the background was subtracted using a straight line from 6800 to 7085 eV. The XANES were normalized using a quartic spline fit through the background. The $\chi(k)$ function was weighted with k^3 to account for damping of oscillations with increasing k. The radial structure function was obtained by Fourier transform of $k^3\chi(k)$ using a k-range of 1.5–16.4 Å^{-1}. The k range was adjusted until the radial structure function exhibited no unexpected peaks below the anticipated Fe–O distance. The EXAFSPAK was also used to fit the EXAFS spectrum with theoretical scattering paths, which were generated with FEFF 8 code [31].

3. Results and discussion

The structure of $LiFePO_4$ has been investigated by a number of groups [32,33]. The structure shows the unit cell containing four $LiFePO_4$ units. The O-sites form a nearly tetrahedral arrangement around the Phosphorus-sites and an approximately octahedral arrangement around each Fe-site. There are channels along the *b*-axis, which can accommodate the mobile Li-ions. When Li^+ are removed electrochemically the remaining $FePO_4$ framework has the same *Pnma* symmetry with a 7% reduced volume [34,35]. There are three different positions and four different interatomic Fe–O distances (2 × 2.2506 Å equatorial, 2 × 2.0639 Å equatorial, 1 × 2.2034 Å axial, 1 × 2.1077 Å axial). The cell had an electrode area of 3.14 cm^2, and was charged at a current density of 1 mA/cm^2, which corresponds to a 3 h charge rate. EXAFS measurements were recorded at different states of charge. Here for clarity we will be presenting the results observed at states of charge A (0.0 mAh), B (0.75 mAh), C (1.5 mAh), D (2.25 mAh) and E (3.0 mAh), respectively. For the potential-time charging curve during the electrochemical oxidation the reader is referred to Deb et al. [29]. The XANES regions of the X-ray absorption spectra are shown in Fig. 1. It shows a rather strong shift of the main edge (Fe 1s → 4p transition and 1s → continuum transition) at the different states (A–E) measured during the charging process, which is mainly due to the change in the valence state of the iron in the sample during the charging process. The 1s electron of the Fe(III) compound is more strongly bonded to the Fe nucleus than in the Fe(II) compound. The edge is shifted by about 4 eV, and this is attributed to the change in valence state of iron in the sample during the charging process. In addition, differences in the weaker forbidden pre-edge transitions Fe 1s → 3d can be seen and the main edge is also structured differently. The shift of the main edge from state A to E is due to the fact that the 1s electron in the Fe^{3+} state is more strongly bonded to

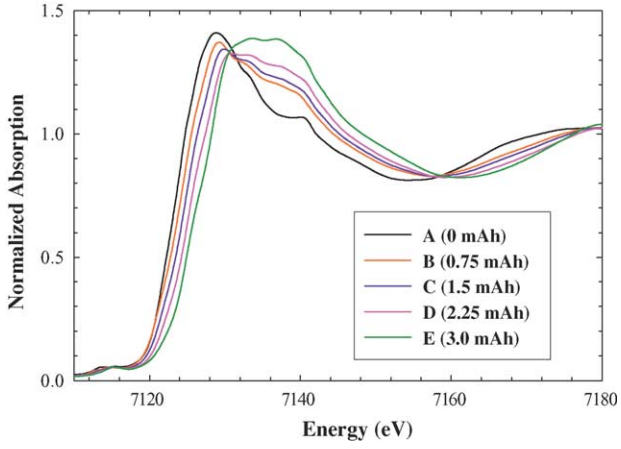

Fig. 1. Calibrated and normalized XANES data at the Fe K edge during charge. The A (0 mAh), B (0.75 mAh), C (1.50 mAh), D (2.25 mAh), and E (3.0 mAh) in the figure represent the different stages in the charge process at which the X-ray measurements were performed.

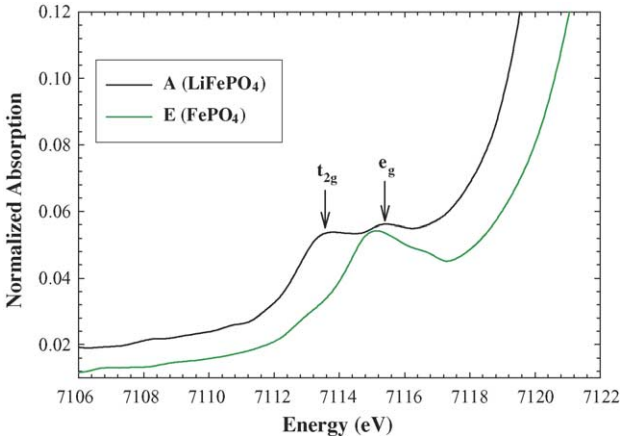

Fig. 2. Pre-edge region of the XAS spectra, which show the t_{2g} and e_g absorption bands at the stages A ($LiFePO_4$) and E ($FePO_4$).

the nucleus than in the Fe^{2+} state. Fig. 2 shows the dipole forbidden pre-edge transitions attributed to Fe $1s \rightarrow 3d$ bands. The ligand field resulting from the phosphate oxygen atoms, which are octahedrally co-ordinated to the iron, splits the 3d states into t_{2g} and e_g states. One can expect additional splitting of these states as the oxygen atoms deviate from the normal octahedral coordination (the Fe–O distances change by about 0.2 Å). Thus the observed splitting of the 3d states resulted from the crystal field splitting of the t_{2g} and e_g energy levels. Previous observation reveals a 2 eV energy difference between the t_{2g} and e_g bands for octahedrally coordinated transition metal compounds [36], which is consistent with our observation here during the charging process from state A–E. Holzwarth et al. [35] showed with their DOS calculations that the ferromagnetic spin configuration (high spin) is the most stable configuration for both the $LiFePO_4$ and $FePO_4$. This is also confirmed by magnetic moment measurements of this compound [37–40]. Analogous to Holzwarth et al. [35] Yamada et al. [14] showed that the 3d electrons of Fe in $FePO_4$ and $LiFePO_4$ are high spin. Since the Fe sites are in approximately octahedral environment the O^{2-} ions split the 3d states into t_{2g} and e_g states and the Fermi level lies in the Fe 3d states. With deviation from the octahedral symmetry, interaction of the O 2p and Fe 3d orbitals causes further splitting of these states. The mixing of the O 2p and the Fe 3d orbitals increases the transition probability of the $1s \rightarrow 3d$ transition (which is dipole forbidden). As the e_g orbitals overlap better with the 2p orbitals, the transition probability to e_g states would be higher. In the case of $FePO_4$ [Fe^{3+}, d^5] it would be more pronounced as the e_g states are less occupied as compared to the Fe (II) compound.

Now turning our attention to the pre-edge feature, the intensity of the pre-edge for the sample at the oxidized state E is similar to that for the sample at state A, indicating that the oxygen atoms retain the octahedral coordination. Here a comparison with appropriate model compounds with well-defined oxidation and coordination states are

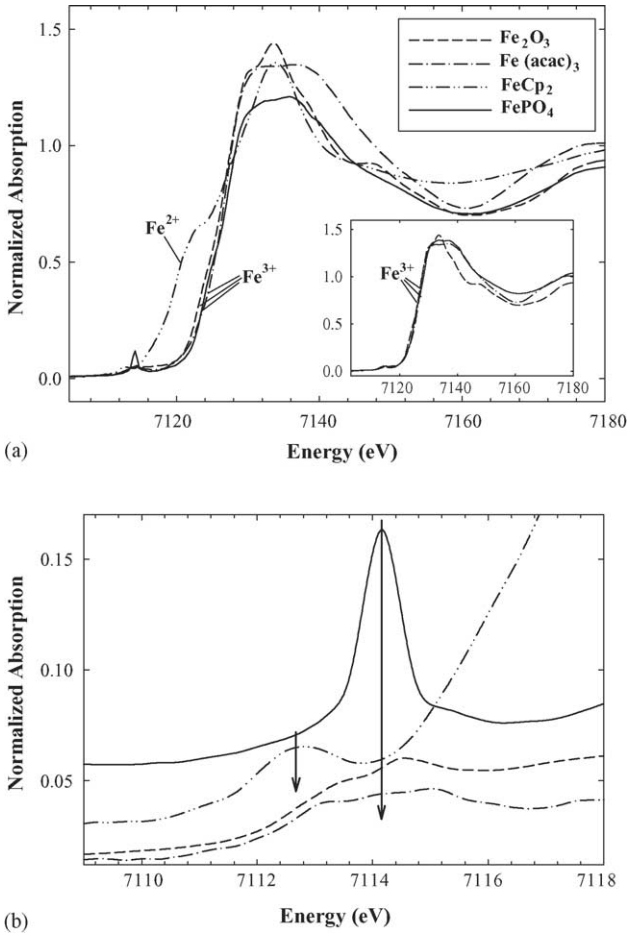

Fig. 3. (a) XANES spectra of the model compounds: Fe_2O_3 (short dash), $Fe(acac)_3$ (dash-dot), $FeCp_2$ (dash-dot-dot) and $FePO_4$ (solid line). The inset shows the comparison of the XANES spectrum recorded at the stage E (solid line), with respect to the other Fe^{3+} model compounds, in octahedral symmetry [α-Fe_2O_3 (short dash) and $Fe(acac)_3$ (dash-dot)]. The axes in the inset are the same as in (a). (b) Magnified $1s \rightarrow 3d$ pre-edge of XANES spectra for the model compounds. The different line codes are the same as in Fig. 3a. The four spectra have been vertically shifted for clarity. The arrows represent the position of the pre-edge peaks.

shown for better understanding of the reader. $FePO_4$ was chosen as an example of Fe^{3+} in tetrahedral coordination and α-Fe_2O_3 and $Fe(acac)_3$ were chosen as examples of Fe^{3+} in octahedral symmetry. $FeCp_2$ has been chosen as an example of a Fe^{2+} compound (where, Cp = cyclopentadienyl, acac = acetylacetonate). $FePO_4$ is usually considered as a perfect model for Fe in tetrahedral co-ordination [41] while $FeCp_2$ is a known stable sandwich compound and the X-ray structure of ferrocene indicated a molecular center of symmetry [41] (D_{5d} symmetry). The XANES spectra of the four model compounds are shown in Fig. 3. The three compounds containing ferric species are observed to exhibit a K-edge at significantly higher energy (7122.3–7123.2 eV) with respect to $FeCp_2$ (7119.3 eV). Though the exact edge position of an element in a material is also defined by the co-ordination ligands and their local symmetry around the absorbing atom (which explains the observed small difference of <0.1 eV,

among $FePO_4$, Fe_2O_3 and $Fe(acac)_3$), the main underlying factor which determines the energy required to induce the photoelectric effect on a 1s electron is the oxidation state of the absorbing atom. Hence, more energy is required to ionize the deshielded metal ion with a higher electron deficit, and this explains the resulting consistent edge shift in the Fe^{2+} compounds with respect of the Fe^{3+} compounds considered here. This interpretation is also true for our observed consistent edge shift in the charging process of the electrode from the initial state A (Fe^{2+}) to the final state E (Fe^{3+}) [Fig. 1]. By electrochemical delithiation during charging of the cell, the stoichiometry changes from Li_xFePO_4 to $FePO_4$, and consequently, iron is oxidized from Fe^{2+} (stage A) to Fe^{3+} (stage E). The corresponding XANES for the stage E, was recorded approximately 3 h after the charging was started. The inset of Fig. 3(a) shows the XANES spectrum of this stage in comparison with the model Fe^{3+} compounds (in octahedral symmetry). The comparison again confirms the fact that iron at stage E ($FePO_4$) is in the Fe^{3+} state. It is also important to mention here that as discussed above, the pre-edge region which is assigned to $1s \rightarrow 3d$ transitions, at the different stages of charging [Fig. 1], shows a weak intensity in this region, indicating an octahedral co-ordination as opposed to the tetrahedral co-ordination for which a strong pre-edge is observed (as in the case of $FePO_4$). Turning our attention to the $1s \rightarrow 3d$ pre-edge feature [Fig. 3(b)], it is seen that the pre-edge is at slightly higher energy for Fe^{3+} compounds than the Fe^{2+} compound. Furthermore, the pre-edge intensity of $FePO_4$ (in tetrahedral symmetry) is relatively intense (at 7114.1) with respect to the Fe_2O_3 and $Fe(acac)_3$ (in octahedral symmetry), where in the case of the latter two compounds the pre-edge is split into two components of much lower intensity. For the Fe^{3+} compounds in octahedral symmetry, the relatively higher intensity observed for Fe_2O_3 results from the higher degree of distortion from the ideal octahedral symmetry with respect to $Fe(acac)_3$. Hence, the pre-edge feature represents the degree of mixing of the 3p and the 3d atomic orbitals to form molecular orbitals. In case of a perfect O_h symmetry the degree of mixing is zero, and it increases as the distortion increases in the O_h symmetry and is higher in case of T_d symmetry, hence explaining the change in the pre-edge features in these model compounds. Now comparing the pre-edge region of this model compound $FePO_4$ (tetrahedral symmetry) which exhibits relatively a higher intensity compared to our oxidized sample at the state of charge E (i.e. $FePO_4$), once again confirming that the Fe (III) state at the final charged state E retains the octahedral coordination of the oxygen atoms. Another interesting feature of the XANES spectra reported here (Figs. 1 and 3) is the intensity of the white line, which is proportional to the coordination of the absorbing atom. The quantitative results obtained from the XANES spectra for the model compounds and also from the different states of charge for the Li_xFePO_4 electrode are summarized in Table 1. To briefly describe the interesting feature on the white lines of the measured XANES spectra, we observe

Table 1
Position and normalized intensity of the observed $1s \rightarrow 3d$ pre-edge peak and of the white line of the XANES for the different model compounds and for different states of charge of Li_xFePO_4 (A, B, C, D and E) during charging of the in situ cell

Sample or charged state	Pre-edge peak		White line	
	Position (eV)	Intensity	Position (eV)	Intensity
	7113.2 (s)	0.044	7133.6	1.42
α-Fe_2O_3	7114.4	0.058		
	7113.3 (s)	0.042	7132.9	1.41
$Fe(acac)_3$	7114.9	0.046		
$FeCp_2$	7112.8	0.051	7133.8	1.40
$FePO_4$	7114.1	0.125	7136.1	1.20
A (0.0 mAh)	7113.3	0.054	7129.2	1.41
B (0.75 mAh)	7113.8	0.053	7130.2	1.38
C (1.5 mAh)	7114.4	0.053	7131.2	1.38
D (2.25 mAh)	7114.9	0.053	7132.3	1.37
E (3.0 mAh)	7115.4	0.055	7133.4	1.39

s: represents shoulder in the XANES spectra.

that white line intensities observed for the different states of charge (A, B, C, D and E) during charging of the in situ cell, shows a similar white line intensity to that observed for the other Fe^{2+} and Fe^{3+} [$FeCp_2$, α-Fe_2O_3, $Fe(acac)_3$] six-fold coordinated (octahedral) model compounds (1.37–1.42; Table 1), much higher than that observed for the four-fold co-ordinated (tetrahedral) model compound [$FePO_4$; 1.20], thus once again reflecting that during charging of the in situ cell iron in Li_xFePO_4 at different charged states are in six-fold co-ordination (octahedral).

Now we will consider the absorption data that are observed at stage A (0 mAh) and the oxidized electrode sample at stage E (3 mAh) to monitor the changes in structure due to the charging of the cell. In Fig. 4 we present the $k^3\chi(k)$-function of the Fe K-edge EXAFS spectrum as a function of k ($Å^{-1}$) after performing standard corrections, which included

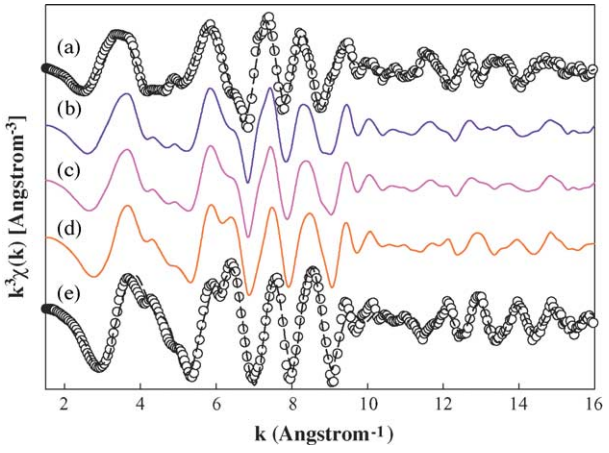

Fig. 4. Observed k^3-weighted [$k^3\chi(k)$] Fe EXAFS at stages (a) A, (b) B, (c) C, (d) D and (e) E during charging. Comparison of the experimental and the FEFF fit theoretical analysis of the k^3-weighted Fe EXAFS spectrum are shown for Fe(II) recorded at the state A and Fe(III) recorded at the state E, for Li_xFePO_4. For both (a) and (e): circles symbol indicate experimental data and broken lines indicate FEFF fit theoretical results.

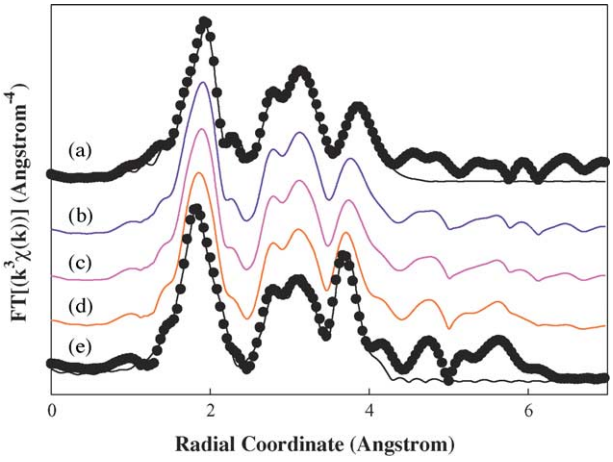

Fig. 5. Comparison of the radial distribution function obtained after Fourier transformation of $k^3\chi(k)$ observed at the stages (a) A, (b) B, (c) C, (d) D and (e) E, respectively. A comparison of the theoretical analysis for the initial state A and final state E are shown here, where circles (filled) symbol indicate experimental data and solid lines indicate FEFF fit theoretical results.

background subtraction, energy calibration, normalization, and weighting of the data with k^3 for the different states of charge. For comparison we have here shown the fit to the EXAFS spectrum with theoretical scattering paths, which were generated with the FEFF 8 code [31] for the state A and E, respectively. Fig. 5 shows the corresponding radial structure function as a function of the inter atomic distance, R (Å), which we obtained by Fourier transformation of $k^3\chi(k)$ over the limited k-space range between 1.5 and 16.4 $Å^{-1}$. The radial structure function shows one strong peak at the start followed by two weaker peaks at higher distances. The peak positions in this radial structure function are close to the radius of the back scattering shells. Quantitative analyses were performed on the first three peaks appearing in the radial structure function between $R = 0.5$ and 4.1 Å. The structural parameters shown in Tables 2 and 3 are obtained from the FEFF fit analysis of Li_xFePO_4 using all possible scattering paths. The coordination atom of the first shell is oxygen,

Table 2
Structural parameters resulting from the FEFF fit for Li_xFePO4 during the initial stage A (0 mAh), derived from fitting the Fe-edge EXAFS spectra

Sphere	$Z_a - Z_b$	CN	R (Å)	σ^2 (Å^2 10^{-3})
k-range = 1.5 – 16.2 $Å^{-1}$				
1st	Fe—O	2	1.991 (2)	1.2 (4)
1st	Fe—O	2	2.122 (3)	2.4 (5)
1st	Fe—O	2	2.264 (5)	4.8 (7)
2nd	Fe—P	1	2.799 (5)	1.8 (1)
2nd	Fe—P	2	3.179 (6)	4.1 (3)
2nd	Fe—P	2	3.299 (2)	6.3 (3)
3rd	Fe—Fe	2	3.813 (2)	4.5 (2)
3rd	Fe—Fe	2	4.187 (6)	6.2 (5)

Numbers in parentheses are statistical errors of the last significant digit. Notes: $Z_a - Z_b$ represents the central absorber and the scattering atom (or path) correlation, CN is the coordination number, R is the inter-atomic distance, σ^2 represent the Debye–Waller disorder parameter.

Table 3
Structural parameters resulting from FEFF fit for Li_xFePO4 during fully charged stage E (3 mAh), derived from fitting the Fe-edge EXAFS spectra

Sphere	$Z_a - Z_b$	CN	R (Å)	σ^2 (Å^2 10^{-3})
k-range = 1.5 – 16.2 $Å^{-1}$				
1st	Fe—O	2	1.793 (5)	1.5 (4)
1st	Fe—O	2	1.996 (8)	2.2 (5)
1st	Fe—O	2	2.201 (5)	4.0 (7)
2nd	Fe—P	1	2.793 (7)	1.7 (1)
2nd	Fe—P	2	3.177 (3)	4.3 (3)
2nd	Fe—P	2	3.186 (7)	6.1 (3)
3rd	Fe—Fe	2	3.794 (2)	4.2 (2)
3rd	Fe—Fe	2	4.166 (6)	6.5 (5)

Numbers in parentheses are statistical errors of the last significant digit. Notes: $Z_a - Z_b$ represents the central absorber and the scattering atom (or path) correlation, CN is the coordination number, R is the inter-atomic distance, σ^2 represent the Debye–Waller disorder parameter.

and that of the second and the third shells are phosphorous and iron, respectively. The best fit was obtained by assuming three different Fe–O distances as shown in Tables 2 and 3, respectively. The Fe–O distances obtained for the two stages A and E varied at the most by 0.2 Å. Using four Fe–O scattering paths did not improve the fit substantially. The best fit was obtained with three Fe–O distances and is shown here. The second peak corresponds to the single scattering paths of Fe–P, corresponding to those obtained from the XRD data in the case of stage A. This is similar to that obtained for the charged stage E while the Fe–P scattering distances varied at the most by 0.1 Å. Comparing all stages between A and E (Figs. 4 and 5) reveals that only subtle changes take place, the structural rearrangement on lithium extraction in Li_xFePO4 is small, as seen from Tables 2 and 3 and the change in Fe–O coordination is minimal: the mean Fe–O distances are 2.13 and 2.01 Å, for $LiFePO_4$ and $FePO_4$, respectively. For a better understanding how the bond distances varies for Fe–O and Fe–P during the charging and discharging, a quantitative analysis using fit results are shown in Fig. 6. As pointed above

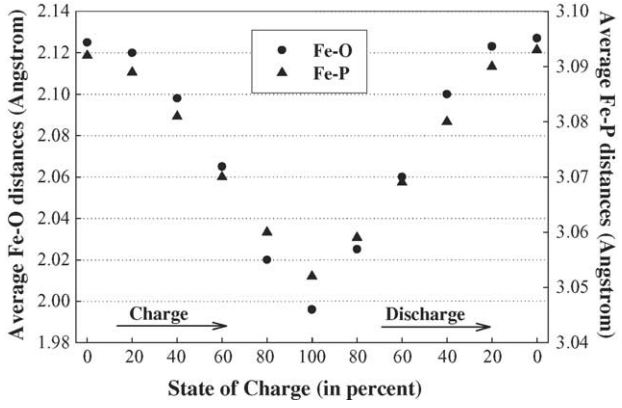

Fig. 6. First shell average metal—oxygen and second shell average metal—phosphorus bond length changes during Li/Li_xFePO_4 cell cycling. The filled symbols (●) and (▲) represent the Fe—O and Fe—P bond distances as observed during different states of charge and discharge.

no single Fe–O distance varies more than by 0.2 Å. This again shows the basis for the truly excellent cycling properties for this system. The results obtained for both stages A and E are in agreement with the crystallographic data, which show that the $FePO_4$ (at stage E) retains the same *Pnma* structure, and there is only a 7% reduction of volume.

4. Conclusions

In conclusion, XAFS has provided us with an excellent tool for analyzing the changes that take place when Li is cycled out of and into Li_xFePO_4 in a Li-ion cell. The XAS analyses indicate that during charging of Li_xFePO_4 to 3.9 V the oxidation state of Fe changes from 2 to 3. The results confirm here that this material possesses very desirable characteristics for an electrode, including small volumetric changes and retention of the Fe–O octahedral symmetry on charging, which makes it an excellent choice for Li-ion cell applications. A comparison with the 1s → 3d pre-edge characteristics of the model compounds also confirms that the Fe and O are octahedrally arranged, as is evidenced by a weak pre-edge intensity, unlike $FePO_4$ where a strong pre-edge intensity is observed due to the tetrahedral co-ordination. The pre-edge intensities at the different states of charge of Li_xFePO_4 show the octahedral arrangement of the phosphate oxygen atoms around each Fe-site is retained. The XANES studies revealed that the $LiFePO_4$ and $FePO_4$ are both in the high spin state and exhibit a crystal field splitting of about 2 eV. The EXAFS data show one strong peak for the first co-ordination shell corresponding to Fe–O scattering contributions and two weaker peaks at higher distances comprise of contributions from Fe–P and Fe–Fe, respectively (Tables 2 and 3). The change in the $R_{Fe–O}$ from the initial stage A (0.0 mAh) to the fully charged state E (3 mAh) varies at the most by 0.2 Å. The results presented here confirm that only minor changes occur in the structure of the electrode during electrochemical cycling.

Acknowledgement

We acknowledge Dr. M. Doeff and Dr. H. Yaoqin, of the Material Science Division, Lawrence Berkeley National Laboratory, for supplying us with the $LiFePO_4$ electrodes. We also acknowledge the help of the staff of the DND-CAT (5-BM-D) beamline at APS. DND-CAT is supported by the E.I. DuPont de Nemours and Co., The Dow Chemical Company, the U.S. National Science Foundation through Grant DMR-9304725 and the State of Illinois through the Department of Commerce and the Board of Higher Education Grant IBHE HECA NWU 96. This work was supported by Director, Office of Basic Energy Sciences, Chemical Sciences Division of the U.S. Department of Energy, under Contract DE-AC03-76SF00098.

References

[1] A.G. Ritchie, J. Power Sources 96 (2001) 1.
[2] M. Nishijima, Y. Takeda, N. Imanishi, O. Yamamoto, M. Takano, J. Solid State Chem. 113 (1994) 205.
[3] L.A. de Piecioto, M.M. Thackeray, Mat. Res. Bull. 21 (1986) 583.
[4] P.H. Domingues, E. Nunez, J.M. Neto, J. Magn. Magn. Mat. 96 (1991) 101.
[5] M. Pernet, P. Strobel, B. Bonnet, P. Bordet, Y. Chabre, Solid State Ionics 66 (1993) 259.
[6] G.A. Fatseas, M. Evain, G. Ouvrard, R. Brec, M.H. Whangbo, Phys. Rev. B 35 (1987) 3082.
[7] A.K. Padhi, K.S. Nanjundaswamy, C. Masquelier, J.B. Goodenough, J. Electrochem. Soc. 144 (1997) 2581.
[8] C. Masquelier, A.K. Padhi, K.S. Nanjundaswamy, J.B. Goodenough, J. Solid State Chem. 135 (1998) 228.
[9] A.K. Padhi, K.S. Nanjundaswamy, C. Masquelier, S. Okada, J.B. Goodenough, Electrochem. Soc. 144 (1997) 1609.
[10] K.S. Nanjundaswamy, A.K. Padhi, J.B. Goodenough, S. Okada, H. Ohtsuka, H. Arai, J. Yamaki, Solid State Ionics 92 (1992) 1.
[11] A.K. Padhi, K.S. Nanjundaswamy, J.B. Goodenough, J. Electrochem. Soc. 144 (1997) 1188.
[12] S. Andersson, J.O. Thomas, B. Kalska, L. Haggstrom, Electrochem. Solid State Lett. 3 (2000) 66.
[13] K. Amine, H. Yasuda, M. Yamachi, Electrochem. Solid State Lett. 3 (2000) 178.
[14] A. Yamada, S.C. Chung, J. Electrochem. Soc. 148 (2001) 960.
[15] A. Yamada, S.C. Chung, K. Hinokuma, J. Electrochem. Soc. 148 (2001) 224.
[16] V.A. Streltsov, E.L. Belokoneva, V.G. Tsirelson, N.K. Hansen, Acta Cryst. B 49 (1993) 147.
[17] A. Bianconi, in: D.C. Konongsberger, R. Prins (Eds.), X-ray Absorption: Principles, Applications, Techniques of EXAFS, SEXAFS and XANES, vol. 573, John Wiley and Sons, New York, 1988.
[18] A. Manceau, A.I. Gorshkov, V.A. Drits, Am. Miner. 77 (1992) 1133.
[19] L.A. Greines, Phys. Rev. B 27 (1983) 2111.
[20] M. Belli, A. Scafati, A. Bianconi, S. Mobilio, L. Palladino, A. Reale, E. Buratini, Solid State Commun. 35 (1980) 355.
[21] G.L. Glen, C.G. Dodd, J. Appl. Phys. 39 (1968) 5372.
[22] M.F. Toney, J. McBreen, Electrochem. Soc. Interf. 2 (1) (1993) 22.
[23] J. McBreen, Electrochim. Acta 47 (2002) 3035.
[24] O. Haas, F. Holzer, S. Muller, J.M. McBreen, X.Q. Yang, X. Sun, M. Balasubramanian, Elctrochim. Acta 47 (2002) 3211.
[25] O. Haas, R.P.W.J. Struis, J.M. McBreen, J. Solid State Chem. 177 (2004) 1000.
[26] M. Balasubramanian, X. Sun, X.Q. Yang, J.M. McBreen, J. Electrom. Soc. 147 (2000) 2903.
[27] C.S. Johnson, A.J. Kropf, Electrochim. Acta 47 (2002) 3187.
[28] J. McBreen, W.E. O'Grady, K.I. Pandya, R.W. Hoffman, D.E. Sayers, Langmuir 3 (1987) 428.
[29] Aniruddha Deb, Uwe Bergmann, Elton J. Cairns, S.P. Cramer, J. Synchrotron Radiat. 11 (2004) 497.
[30] M.M. Doeff, Y. Hu, F. McLarnon, R. Kostecki, Electrochem. Sol. State Lett. 6 (2003) 207.
[31] A.L. Ankudinov, B. Ravel, J.J. Rehr, S.D. Conradson, Phys. Rev. B 54 (1998) 7565.
[32] A. Yamada, S.Ch. Chung, K. Hinokma, J. Electrochem. Soc. 148 (2001) 224.
[33] V.A. Streltsov, E.L. Belokoneva, V.G. Tsirelson, N.K. Hansen, Acta Cryst. B 49 (1993) 147.
[34] A.S. Andersson, J.O. Thomas, J. Power Sources 97-98 (2001) 498.

[35] P. Tang, N.A.W. Holzwarth, Phys. Rev. B 68 (2003) 165107.
[36] M. Pouchard, A. Villesuzanne, J.-P. Doumerec, J. Solid State Chem. 162 (2001) 282.
[37] R.P. Santoro, R.E. Newnham, Acta Crystallogr. 22 (1967) 344.
[38] J.G. Creer, G.J. Troup, Phys. Lett. A 32 (1970) 439.
[39] M.C. Tucker, M.M. Doeff, T.J. Richardson, R. Finones, E.J. Cairns, J.A. Reimer, J. Am. Chem. Soc. 124 (2002) 3832.
[40] H.N. Ng, C. Calvo, Can. J. Chem 53 (1975) 2064.
[41] P.F. Eiland, R. Pepinsky, J. Am. Chem. Soc. 74 (1952) 4971.